

In-flight calibration of Hitomi Soft X-ray Spectrometer. (1) Background

Caroline A. KILBOURNE,^{1,*} Makoto SAWADA,² Masahiro TSUJIMOTO,³
Lorella ANGELLINI,¹ Kevin R. BOYCE,¹ Megan E. ECKART,¹ Ryuichi FUJIMOTO,⁴
Yoshitaka ISHISAKI,⁵ Richard L. KELLEY,¹ Shu KOYAMA,³
Maurice A. LEUTENEGGER,^{1,6} Michael LOEWENSTEIN,^{1,7} Dan MCCAMMON,⁸
Kazuhisa MITSUDA,³ Shinya NAKASHIMA,⁹ Frederick S. PORTER,¹
Hiromi SETA,⁵ Yoh TAKEI,³ Makoto S. TASHIRO,¹⁰ Yukikatsu TERADA,¹⁰
Shinya YAMADA,⁵ and Noriko Y. YAMASAKI³

¹NASA/Goddard Space Flight Center, Greenbelt, MD 20771, USA

²Department of Physics and Mathematics, Aoyama Gakuin University, 5-10-1 Fuchinobe, Chuo-ku, Sagami-hara, Kanagawa 252-5258, Japan

³Japan Aerospace Exploration Agency, Institute of Space and Astronautical Science, 3-1-1 Yoshinodai, Chuo-ku, Sagami-hara, Kanagawa 252-5210, Japan

⁴Faculty of Mathematics and Physics, Kanazawa University, Kakuma, Kanazawa, Ishikawa 920-1192, Japan

⁵Department of Physics, Tokyo Metropolitan University, Hachioji, Tokyo 192-0397, Japan

⁶University of Maryland – Baltimore County, Baltimore, MD 21250, USA

⁷University of Maryland, College Park, MD 20742, USA

⁸Department of Physics, University of Wisconsin, Madison, WI 53706, USA

⁹Institute of Physical and Chemical Research, Wako, Saitama 351-0198, Japan

¹⁰Department of Physics, Saitama University, Sakura-ku, Saitama, Saitama 338-8570, Japan

*E-mail: caroline.a.kilbourne@nasa.gov

Received 2017 July 10; Accepted 2017 November 1

Abstract

The X-Ray Spectrometer (XRS) instrument of Suzaku provided the first measurement of the non-X-ray background (NXB) of an X-ray calorimeter spectrometer, but the data set was limited. The Soft X-ray Spectrometer (SXS) instrument of Hitomi was able to provide a more detailed picture of X-ray calorimeter background, with more than 360 ks of data while pointed at the Earth, and a comparable amount of blank-sky data. These data are important not only for analyzing SXS science data, but also for categorizing the contributions to the NXB in X-ray calorimeters as a class. In this paper, we present the contributions to the SXS NXB, the types and effectiveness of the screening, the interaction of the screening with the broad-band redistribution, and the residual background spectrum as a function of magnetic cut-off rigidity. The orbit-averaged SXS NXB in the range 0.3–12 keV was 4×10^{-2} counts s⁻¹ cm⁻². This very low background in combination with groundbreaking spectral resolution gave SXS unprecedented sensitivity to weak spectral lines.

Key words: instrumentation: spectrographs — methods: observational — space vehicles: instruments

1 Introduction

While it is feasible to perform many aspects of calibration on the ground before the launch of astronomical instruments, the investigations of the instrumental background before launch mainly serve as previews and to define initial screening algorithms. The Soft X-ray Spectrometer (SXS: Kelley et al. 2016) onboard the Hitomi satellite (Takahashi et al. 2016) performed well up to the premature end of the mission due to loss of the spacecraft control, meeting or exceeding its requirements (including achieving ~ 5 eV FWHM energy resolution) and yielding new insights into the Universe. Although the commissioning phase was not completed, leading to larger systematic uncertainties in energy scale than would have been achievable, a robust measurement of the SXS non-X-ray background (NXB) was obtained. The resulting background data set represents a substantial improvement over the lone prior measurement of the NXB in an X-ray calorimeter array, which was measured on the Suzaku X-Ray Spectrometer (XRS) in 2005 for only 37 ks and with no constraint on attitude (Kilbourne et al. 2006; Kelley et al. 2007). The Hitomi SXS residual background that we present in this paper was obtained from 366 ks of Earth eclipse data obtained after temperature stability had been attained. The SXS gate valve was never opened, thus a 0.26 mm-thick Be window was in place over the aperture for all of this time.

The following description of the configuration of the SXS calorimeter array and its associated anti-coincidence detector sets the foundation for understanding the immediate physical environment in which the background signals were produced. The 36 pixel SXS calorimeter array consisted of micro-machined, silicon thermometers and separately attached HgTe X-ray absorbers, arrayed on a 0.83 mm pitch. Improvements relative to the Suzaku XRS array are covered elsewhere (Kilbourne et al. 2016), but a significant change that must be mentioned in discussing the background was the addition of a $1.5 \mu\text{m}$ layer of Au to areas on the top and bottom of the silicon frame of the array for heat sinking. The regions on the top were thermally connected to thicker Au on an alumina fan-out board by a series of Au wire bonds, and the fan-out board was similarly connected to the 50 mK heat sink. One of the pixels in the 6×6 array was not read out in order to use its amplifier (channel 12) for a dedicated calibration pixel located outside of the aperture. A highly collimated ^{55}Fe source (Chiao et al. 2016) mounted in the lid of the detector housing continuously illuminated this pixel in order to provide a gain reference.

In order to veto signals produced by minimum ionizing particles, a Si ionization detector designed to operate at 50 mK was placed behind the calorimeter array. This

anti-coincidence (anti-co) detector (Kilbourne et al. 2016) covered 1 cm^2 , was 0.5 mm thick, and the separation between its top surface and the plane of the array was 0.63 mm. The signals from both the calorimeter array and the anti-co were amplified, filtered, and digitized in the amplifier electronics (XBox) and sent to the digital processor (PSP: Ishisaki et al. 2016) for basic event characterization and pulse-height analysis. The anti-co signals were telemetered as events to allow maximum flexibility in determining the appropriate veto algorithm, instead of setting anti-co flags on events in flight. Figure 1 is a schematic of the detector stack. Photographs showing the actual coverage of the heat-sinking regions and many other details can be found in Kilbourne et al. (2016).

Every calorimeter event is classified by a grade, which indicates both how close the event was to another event and how it was processed (Boyce et al. 1999; Seta et al. 2012). A high-resolution (H) event is separated from both the prior and subsequent event on the same pixel by at least 70 ms and can be analyzed using the full pulse record and digital filter, a mid-resolution (M) event is processed using a shorter record, and a low-resolution (L) event is too close to another event to use the whole pulse in the analysis, and thus is assigned an energy based on its pulse height. The designation “primary” (p) or “secondary” (s) is used to indicate whether the event is the second of consecutive close events. The five grades are abbreviated as H, Mp, Ms, Lp, and Ls, and are also identified numerically as ITYPE 0–4. Grades are relevant to the background discussion because the determination of arrival time, rise time, and energy depends on grade, especially for non-standard pulse shapes.

Throughout this paper, we used the HEASoft software and CALDB (calibration data base) released on 2017 May 12 for the Hitomi collaboration with pipeline data products version 03.01.006.007 (or the 2016 December 30

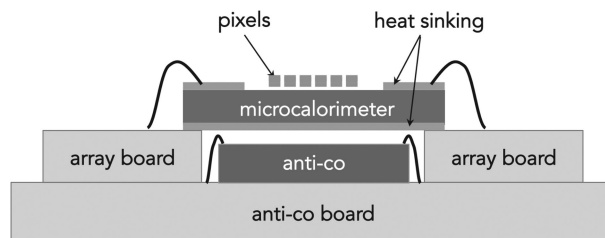


Fig. 1. Schematic showing the geometrical arrangement of the SXS calorimeter array and anti-coincidence detector, shown in cross-section. Features are not to scale. Highlighted are the HgTe X-ray absorbers of the pixels, heat-sinking regions on the array frame, the fan-out boards, and representative wire bonds. Not shown is the hole in the frame under the thermistor of each pixel (thus making an array of square holes), nor the limited extent of the heat-sinking layer on the top, in order to avoid the electrical contacts to the pixels.

release, which is equivalent for background data, since the energy-scale calibration was unchanged), except where noted. The various screening cuts discussed in this paper are enabled in the pipeline processing via the setting of various status flags based on parameters in the CALDB. For example, STATUS[3] is the anti-co flag, set according to the timing parameters in CALDB. Standard or observation-specific screening involves selecting events based on those status flags.¹

2 Background analysis

2.1 Overview of data, analysis approach, and products

Determination of the NXB is an iterative process. The first step is to look at a nominally source-free data set and to study it with only the minimal screening applied, such as the removal of events that were not fully processed or the use of GTI (good time intervals) to exclude crossings of the South Atlantic Anomaly (SAA) or intervals outside of the nominal operating temperature range. The goal of the first pass is to establish and subsequently refine the screening criteria for removing potential background events. The second task is to apply those screening criteria to data from calibration and astrophysical sources to assess whether any systematic loss of real data is incurred, to adjust the screening criteria if shown to be necessary. Lastly, once the screening criteria are established, the final NXB data sets are made available to observers, along with tools for producing an NXB spectrum appropriate to the data cuts and orbital parameters of a particular observation. In the following sections, we explain our findings in each of these analysis phases.

There are four broad classes of background events in a calorimeter array. Any deposition of energy into a pixel registers a normal pulse signal, whether that energy comes from a photon, an absorbed particle, or a minimum ionizing particle (MIP), thus the only possibility for rejecting background events in this class is via coincidence. Secondly, a large deposition of energy into the support frame around the array can result in a disturbance of the heat-sink temperature that produces signal pulses on multiple pixels. Such “frame events” can be identified by pixel-to-pixel coincidence and potentially by pulse shape. The third and fourth classes are thermal and electrical crosstalk, which, if present, are identified by coincidence and pulse-height ratios for nearest-neighbor pixel or electrical-channel

pairs, and potentially by pulse shape as well. A physical understanding of the origin of each class and subclass of rejectable background is not strictly necessary for developing good screening criteria. However, in order to plan for future missions, such understanding is essential. While a complete model of the sources of background and their interaction with the detectors is beyond the scope of this paper, we will present our current understanding and its basis.

2.2 Classes of background events and determination of screening criteria

2.2.1 Anti-coincidence-flagged events

The most important class of rejectable background events to identify consists of events that produce a signal in both a calorimeter pixel and the anti-co. For these, the essential screening parameters are relative timing and threshold (and minimum time above threshold) for the anti-co pulses. Preliminary values for these parameters were determined on the ground using the coincident signals from atmospheric muons, which are a convenient, though low-rate, population of MIPs. The calorimeter and anti-co signals were shaped and triggered differently, thus there was a small offset in the times of coincident events in the raw telemetry. This offset was different for several of the pixels and it also depended on event grade, thus studies of the timing of MIP events on the ground were used to establish relative timing corrections that needed to be applied by pixel and by grade to the calorimeter events. A slight dependence of this offset on the energy of the anti-co pulse was ignored. After absolute timing was established through analysis of the SXS observation of the Crab pulsar (K. Koyama et al. in preparation), the data pipeline corrected the times of all the calorimeter events, but not the anti-co events. Thus, the condition for anti-co coincidence (STATUS[3] = 1 in the event file) was defined by an offset and a 1-ms-wide window. The window width was roughly twice larger than required to provide additional margin on background rejection at little cost in throughput.

2.2.2 Crosstalk

The relative magnitude of thermal crosstalk was measured to be $<10^{-4}$ for nearest neighbors and diminished with increasing separation, thus thermal crosstalk did not play a role in either background or noise. The scale of electrical crosstalk, in contrast, was measured at 6×10^{-3} between adjacent wire pairs in the feedthrough to the cold pre-amplifier, though the digital filter and energy scale combine to suppress that by a factor of ~ 3 . Thus, electrical crosstalk is only a potential background component at very low energies in hard sources. Additionally, electrical

¹ For more detail on the STATUS flags and other screening, please see (https://heasarc.gsfc.nasa.gov/docs/hitomi/analysis/hitomi_analysis_guide_20170306.pdf).

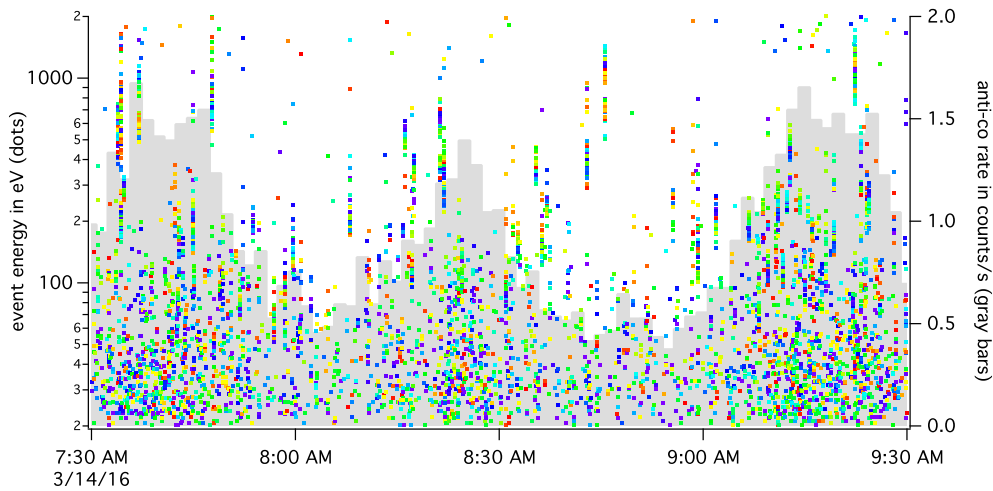


Fig. 2. Energies of triggered events versus time over a three-hour period of Hitomi sequence 100042040 are indicated by dots that are shaded to indicate the signaling pixels (pixel 0 = red, pixel 35 = violet). The gray-shaded histogram in the background indicates the count rate on the anti-coincidence detector. Vertical streaks show groups of coincident events, the rate of which increases with decreasing energy. (Color online)

crosstalk pulses have shorter rise times, which could be used as a discriminator, although rise-time determination becomes increasingly noisy as pulses become smaller. We will address screening by rise time in the next section.

2.2.3 Other correlated events

In SXS ground data, about half of the pixel-to-pixel correlations involved the calibration pixel. The rate and calibration-pixel energies were not consistent with random coincidence, and the sum of the energies of the two events was <6.5 keV, the energy of the Mn $K\beta$ line (and most of the time less than the Mn $K\alpha$ line) illuminating the calibration pixel. This phenomenon was observed on XRS (Kilbourne et al. 2006), and appears to be due to photo-electrons lost from the calibration pixel being absorbed by pixels in the array. This phenomenon, more generally, is discussed in subsection 2.3. Additionally, there was a small but significant number of correlations of events on 2–3 physically near pixels, and nearly all of these involved at least one event >10 keV. This class has not yet been explained; similar events seen in orbit are noted in sub-subsection 2.4.3.

Notably, in SXS ground tests, there were no large groups of correlated events such as the frame events seen by XRS even on the ground (Stahle et al. 2004) and that filled its telemetry on Suzaku. For SXS, in a typical 12-hr period allocated to a background integration on the ground, there was ~ 1 larger group of events that could have as easily been interference as evidence of a background process. On the XRS arrays, a MIP traversing the silicon frame deposited enough energy to create a triggered event; the relationship between deposited energy and apparent pulse energy had been demonstrated by irradiating the frame of an XRS array

with 5 MeV alpha particles. The main reason for adding the gold heat sinking to the SXS array had been to eliminate these events, and ground testing showed that the remedy had been effective. Irradiating a corner of the frame of an SXS test array with 5 MeV alpha particles produced no signal, and the scale of signals produced by pulsing a heater on the frame was consistent with the lack of response to the alpha particles.

Nonetheless, in orbit, SXS unfiltered data did contain clusters of events reminiscent of the XRS frame events. Figure 2 shows an example from observation sequence 100042040 (nominally IGR J16318–4848, but the target was outside of the field of view). The rate of event clusters tracks the particle rate seen by the anti-co. The energies assigned to the pulses of a frame event are similar in scale, and, for a given anti-co rate, the rate of event clusters increases with decreasing pulse height. An equivalent plot for XRS would contain orders of magnitude more events, but it would appear qualitatively similar to the SXS plot if the energies of the XRS events were divided by a factor of ~ 20 . Thus, it appears that SXS was a factor of 20 less sensitive to frame events than XRS.

Another important difference between the SXS and XRS frame events is the shape of the associated events. The temperature of a pixel is elevated above the heat-sink temperature by its electrical bias power and any radiative loading. When the temperature of its heat sink is pulsed, the pixel temperature will follow that change but will be filtered by its thermal response function. On XRS, the impulse response of the frame resulted in frame events that were indistinguishable from absorber events, thus coincidence was the only tool for identifying them. On SXS, there appeared to be correlated events with both faster and slower

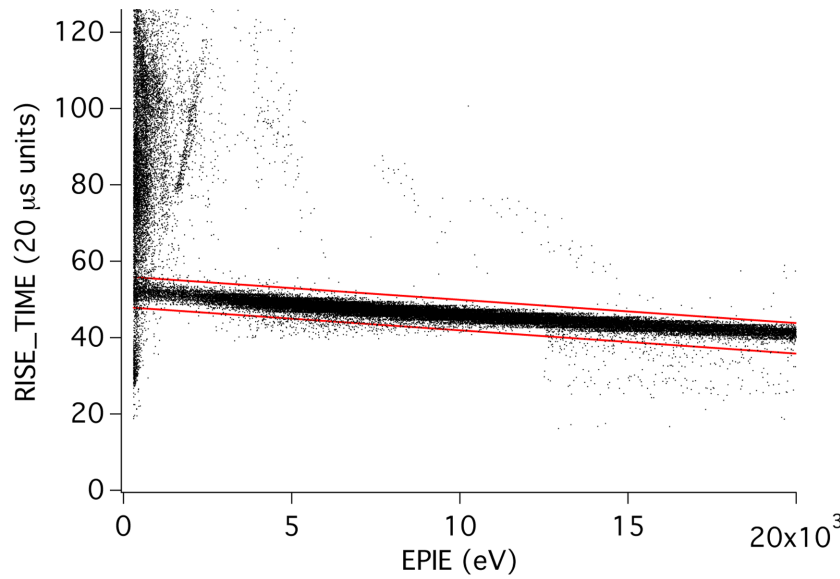


Fig. 3. Saturated plot of RISE_TIME versus EPIE (energy) of the SXS NXB prior to screening. A dot marks each event, and the solid lines show the recommended data cut around the phase space where normally shaped events appear. A random number between ± 0.5 was added to each RISE_TIME value to make the plot easier to read. (Color online)

rise times. Before accumulating the statistics to be able to discuss the characteristics of these events (summarized in subsection 2.4), we established a rise-time cut to eliminate as many of them as possible, as well as other spurious signals, even without coincidence analysis. Figure 3 is a saturated plot of RISE_TIME versus EPIE for the unscreened NXB, all grades included. The parameter RISE_TIME is the interval between the maximum of the pulse derivative and its zero crossing in units of $20 \mu\text{s}$, and EPIE is the event energy in eV converted from pulse height using an energy scale that extends beyond the nominal range. Rise times tend to get shorter with energy because of the non-linearity of the detector. Figure 3 shows the events as dots and the recommended rise-time cut of

$$(((\text{ABS}(\text{RISE_TIME} - 52 + \text{EPIE} * (52 - 42) / 16383.75)) \leq 4) \&\& \text{ITYPE} < 4) \mid \mid (\text{ITYPE} == 4))$$

where ITYPE indicates the event grade. The ITYPE test omits the cut for Ls events, for which the rise time is distorted by pile up.

In order to screen for pixel-to-pixel coincidence, a time window needed to be established. Based on interval statistics in ground data, a window of 0.24 ms was provisionally established, but to capture the frame events adequately, this window needed to be expanded. One contribution to the assignment of time comes from how much the PSP needs to shift the optimal filter template to obtain the largest value for the pulse height, and this process will give erroneous relative arrival times for pulses with different rise times. Because most frame events can be removed

by the rise-time cut, the coincidence window only needed to be expanded enough to identify frame events that were assigned rise times in the acceptable range. Figure 4 shows how the window was determined using data from the observation of RX J1856.5–3754, which was undetectable by SXS with the gate-valve closed. The data were processed with the 2016 June 24 release of the Hitomi software. Histograms were made of the occurrences of time intervals between consecutive events including (1) all array events over 150 eV, (2) only intervals between events with at least one with a good rise time, and (3) only intervals between events, both with good rise times. For this exercise, a simplified rise-time window of 42–56 was used. A window of 0.72 ms was chosen for pulses on pixels within the array, based on the second case. For coincidence with the calibration pixel, the window was reduced to 0.24 ms, as indicated by the third case and by ground testing, to minimize false coincidence with events from the internal calibration source. Dead time was further reduced by checking whether the energies of the calibration-pixel event and the event coincident with it were consistent with electron loss from the calibration pixel.

The flagging of pixel-to-pixel correlations is done prior to any rise-time cut, to preserve the ability of events with bad rise times to identify group members that pass the rise-time screening. In order to avoid a need for special treatment of electrical cross talk, which would entail identifying such an event and then not flagging its parent for removal, we set an energy threshold on the pixel-to-pixel correlation test. We conservatively set that threshold at

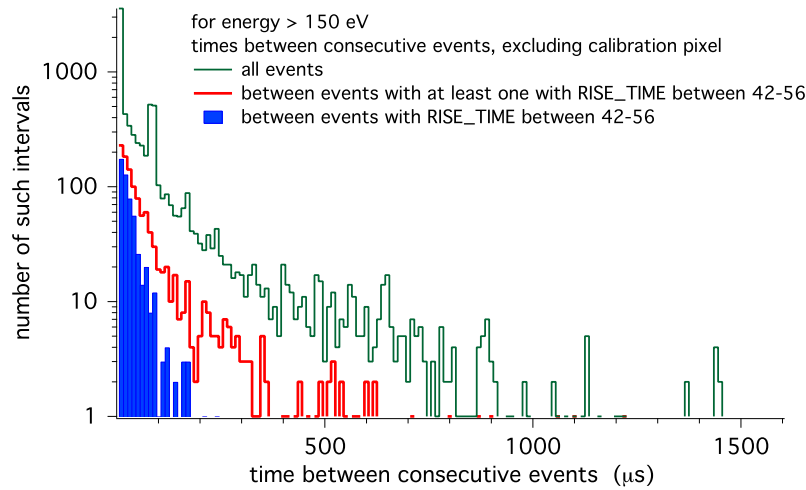


Fig. 4. Interval statistics from “blank sky” data, showing how the range of interval times increases as events of more varied rise times are included. Since we only need to use coincidence to identify correlated events within the good rise-time range, intervals between two events with bad rise times can be omitted from consideration. Thus, 0.72 ms was chosen as the coincidence window between pulses on pixels within the array, based on the middle (red) histogram. (Color online)

300 eV (PI = 600, where PI is energy bin number) to exclude cross talk of all grades resulting from neighboring events of energies up to 32 keV.

2.3 Interaction of screening with broad-band spectral redistribution

Electron loss is mainly considered a component of spectral redistribution (Eckart et al. 2016; M. A. Leutenegger et al. in preparation), but because some of the lost electrons are detected by other pixels, a fraction of this continuum will be removed by the background screening. In order to quantify this effect, we studied close pairs of events (separation <0.24 ms) in the data taken with the filter-wheel ^{55}Fe source rotated into the aperture (sequence 100043030). Of 561175 events analyzed, only 289 pairs (578 events) had energies consistent with being an electron-loss pair associated with an ^{55}Fe photon. Thus, screening them would remove 0.1% of the events. The photon flux in the electron-loss continuum produced by 6 keV photons is about 3% of the flux in the line, which means that these pairs identify roughly 3% of the electron-loss continuum. Screening such pairs is only important in cases of high contrast, such as from the calibration pixel to the array, or from a bright central object to its outskirts.

2.4 Characteristics of the raw and residual SXS NXB

2.4.1 The NXB data set

We constructed an NXB data set by combining earth-eclipse data for the periods before and after March 4 separately.

Table 1. Exposure of the NXB data set in different COR ranges.

COR range	Exposure (s)
<6	1.76×10^4
6–8	3.13×10^4
8–10	5.97×10^4
10–12	9.40×10^4
>12	1.63×10^5

Because of the gain changes in the early part of the mission and the larger systematic uncertainties in the energy scales at that time, we are presenting only the results from the data after March 4. We found no difference between the background spectra of the day and night portions of eclipse, thus we have combined them for 365968 s of exposure. We note, however, that this is unlikely to have been true after the gate valve was opened. The distribution of exposure among different ranges of magnetic cut-off rigidity (COR) is shown in table 1.

The standard reference NXB data made available to observers were processed with standard cleaning, which omits any cuts on rise time, pixel-to-pixel coincidence, or event grade. Use of these cuts needs to be tailored to the rate and energy band of particular observations, and thus is left open so that the same cuts can be applied to the source and background files. In order to assess the efficacy of all the background screening, we also produced a raw NXB event file that had not been cleaned of coincidences with the anti-co or calibration pixel.

The total spectrum measured by the anti-co during the same time intervals is shown in figure 5. The broad peak at 200 keV corresponds to the energy deposited by a MIP proton traversing the detector at normal incidence. The peak at 69 keV is most likely Au $K\alpha$ fluorescence from the heat sinking on the back of the array. The trigger threshold was set to 10 keV, but only events with more than one point above the threshold ($\text{DURATION} > 1$) and with energy > 30 keV were used in coincidence screening, to avoid noise triggers and hard X-rays. The average rate of such events at the 1 cm^2 device was $0.73 \text{ counts s}^{-1}$.

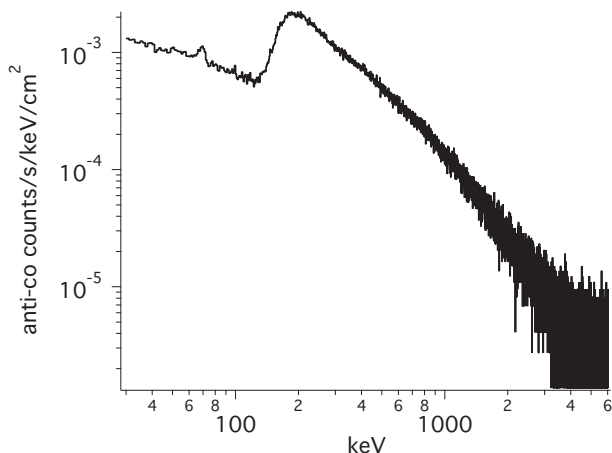


Fig. 5. Total spectrum of the SXS anti-coincidence detector over the same time intervals over which the NXB data set was extracted. Only events meeting the same criteria as applied to coincidence screening (energy > 30 keV and $\text{DURATION} > 1$) are included.

2.4.2 Properties of the residual NXB

For any observation, the NXB needs to be constructed based on the COR exposure during that observation, and cleaned in the same way as the target data (e.g., grade selection and rise-time cut). To provide the reader some sense of the typical residual background, however, in figure 6 we show the residual background spectrum for the entire data set with what would have become standard screening for low-surface-brightness objects. This cleaning included screening for coincidence with the anti-co, screening for pixel-to-pixel coincidences as discussed in sub-subsection 2.2.3, performing the energy-dependent rise-time cut, and keeping only H and Mp events. The total flux from 0.3–12 keV is $4 \times 10^{-2} \text{ counts s}^{-1} \text{ cm}^{-2}$, from 1–10 keV is $3 \times 10^{-2} \text{ counts s}^{-1} \text{ cm}^{-2}$, and from 12–32 keV is $4 \times 10^{-2} \text{ counts s}^{-1} \text{ cm}^{-2}$. Several prominent fluorescent lines are clear. The strongest is a Mn $K\alpha$ line that was seen at the same rate on the ground, and must originate from X-rays scattering in the Be window at the tip of the collimated source pointed at the calibration pixel. The distribution across the array is not uniform, as shown in figure 7. The next most prominent lines are Au fluorescence. Only the Mn $K\alpha$ line was bright enough to provide a check on energy scale during observations, and only on the array as a whole. Aside from the overall rate, there was no significant difference between the NXB spectra that were selected by COR. Figure 8 shows the soft and hard NXB rates for the COR regions of table 1. The spectrum with the highest rate, at the lowest COR, appears marginally softer than the other regions.

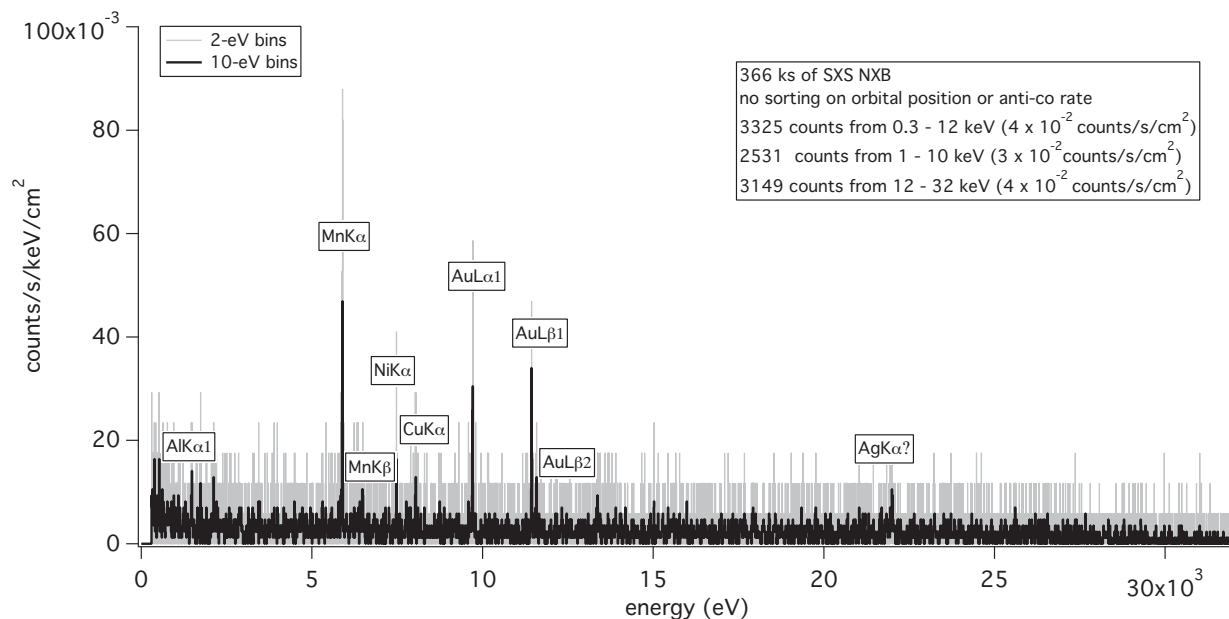


Fig. 6. Spectrum of the residual NXB for the entire reference data set, after standard screening (see text).

2.4.3 Properties of the raw NXB and effectiveness of the individual screening steps

It is useful to introduce the concept of the raw NXB, which consists of the events during earth occultation that have been cleaned only of bad events and for GTI. We establish the difference between bad events and screenable NXB events as follows. Bad events are events, such as very close pile up or interference signals, that should be rejected in all cases. NXB screening is more subjective. Coincidence windows and rise-time ranges are based on population statistics and can be refined for the needs of specific observations or analysis priorities. The standard screening for SXS was based on the limited data obtained, and it is likely that continued operation would have resulted in refinement of the

process. Thus, in what follows, we contrast the raw NXB with the residual NXB that is left after various screening steps are performed.

Figure 9 compares the raw reference NXB spectrum without any coincidence or rise-time screening to the reference residual NXB shown in figure 6. The graph in figure 9 shows the raw reference NXB both for all grades and H+ Mp only. Many of the slow frame events trigger as Lp/Ls pairs, due to the difference between their pulse shapes and the reference pulse used in searching for secondary triggers, thus a substantial amount of the background below 2 keV would be removed simply by rejecting Lp and Ls events. The peak at ~ 6 keV corresponds to a MIP proton traversing a HgTe absorber of $10\ \mu\text{m}$ thickness at normal incidence.

The most important screening to remove background events is achieved by removing events coincident with events on the anti-co (STATUS[3]). This first cut removes 77% of the NXB over 0.3–12 keV. The next most important population of events to remove consists of frame events that are not coincident with the anti-co. Screening on pixel-to-pixel coincidence (STATUS[4]) removes 61% of the remaining events, and 5% of those remaining after that are removed by excluding coincidences with the calibration pixel that meet the energy test (STATUS[6]). The standard rise-time cut at the end removes 15% of the events that survive the series of coincidence tests. Of the final residual background, $<1\%$ of the events are not H or Mp, showing that the background events that can be screened by grade are effectively screened by the other cuts. Both the STATUS[4] and rise-time cuts target the frame events, and

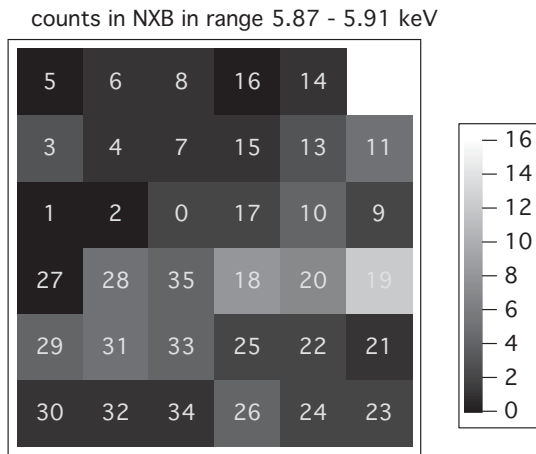


Fig. 7. Distribution of the Mn $K\alpha$ background line across the array in 366 ks. Each pixel is labeled by its channel identification.

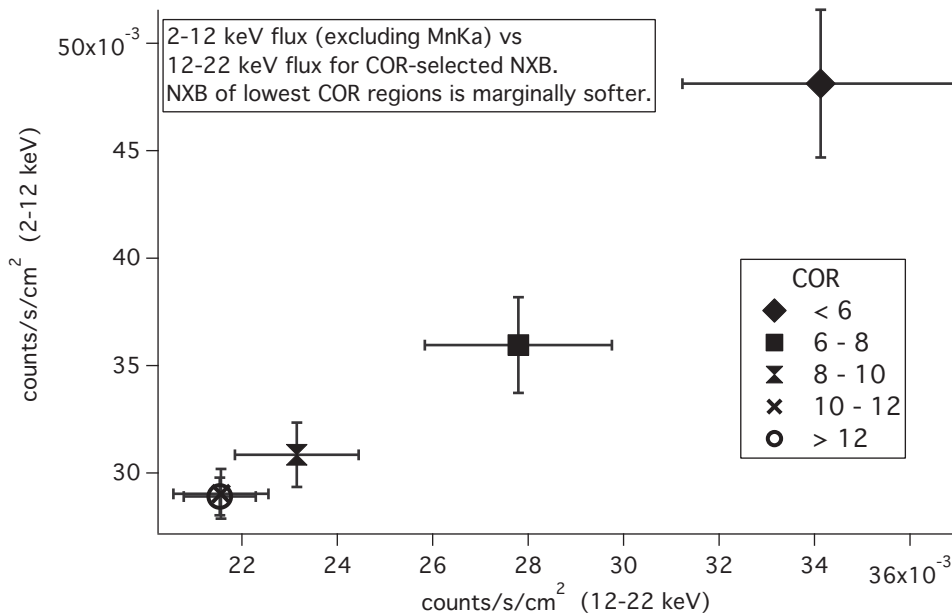


Fig. 8. COR-selected residual NXB rates: 2–12 keV and 12–22 keV.

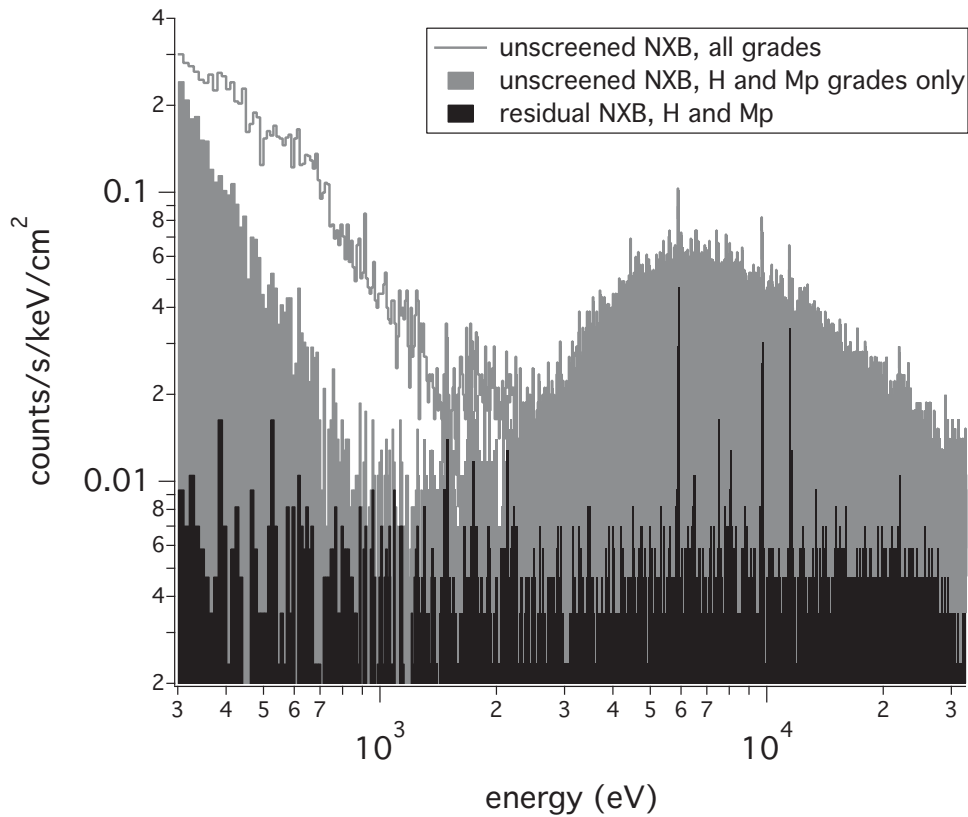


Fig. 9. The raw reference NXB spectrum without any coincidence or rise-time screening (gray-outlined histogram) is compared with the reference residual NXB (filled black histogram) shown in figure 6. A raw reference NXB for grades H + Mp only is also shown (filled gray histogram). From 0.3–12 keV, the residual NXB is 7.3% of the full raw NXB.

the two approaches are largely but not completely overlapping. If in the series above the STATUS[4] and rise-time cuts are swapped, their incremental results are comparable. The rise-time cut is slightly more effective below 1 keV, while the STATUS[4] cut is better above 1 keV. Note that the STATUS flags are set prior to any cuts, so the order of the cuts does not affect the final result.

In order to test whether the STATUS[4] events were consistent with our understanding of frame events and the thermal properties of the array, we studied the rate, multiplicity, and spatial arrangement of correlated groups. We found that most groups were only pairs of events, with only 40% of groups involving more than two pixels. The rate of pairs was not consistent with false coincidence in the unscreened NXB. For low-energy pairs ($\lesssim 2$ keV), the energies of the two events were correlated, rise times were slow, and the pixels involved were spatially correlated. Thus, these events appear to be classic frame events that are limited in multiplicity by a threshold effect, which is consistent with the rise-time cut being a more effective way to screen the background at low energies than pixel-to-pixel coincidence. Higher energy pairs, while still spatially correlated, had normal rise times and were less tightly correlated in

energy. High-multiplicity groups tended to consist of physically contiguous pixels, often all on one side or corner, but sometimes arranged in streaks through the array.

For diagnostic purposes, in addition to the event data, the PSP telemetered whole pulse records at a lower rate and priority. We correlated these pulses with the STATUS[4] events in order to visualize the event classes. There were only 83 pulse dumps that could be associated with any of the 5923 STATUS[4] events in the standard reference NXB data, so the resulting picture is necessarily qualitative. Figure 10 shows three pulse records associated with a group that involved 21 pixels. A pulse from the calibration pixel is included as a reference for a normal pulse shape; the correlated events take more time to rise and fall than a normal pulse. All pulse dumps associated with groups with large multiplicity had similar pulse shapes. Most pairs looked like normal pulses, except for a few with energies close to 300 eV. A few pairs from physically close pixels had slightly faster rise and fall times, suggesting a local frame disturbance that dissipated faster than the internal equilibration times of the pixels.

Classic frame events, resulting from energy deposition into the silicon around the array, likely correspond to a

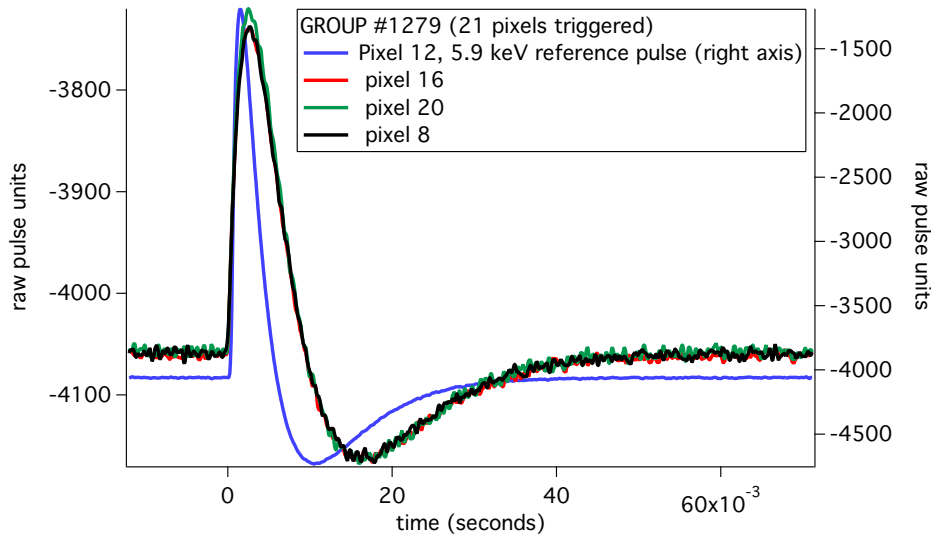


Fig. 10. Pulse records that were telemetered for three out of 21 correlated events in the raw NXB. A normal pulse is included as a reference. (Color online)

population of particles similar to those that trigger the anti-co; thus, by comparing rates, we can estimate the effective sensitivity of the array to such particle hits. Identifying frame events as groups with a maximum energy < 1.75 keV and $\text{RISE_TIME} > 50$, we determined the rate of frame events into the 1.5 cm^2 frame to be $1.1 \times 10^{-3} \text{ s}^{-1} \text{ cm}^{-2}$. Including events as low as 100 eV in flagging correlation, the number of frame events increases by about a factor of 2.3, though properly classifying events below 300 eV is increasingly subjective. If we increased the trigger threshold on the anti-co until its rate became comparable to the apparent frame-event rate in the nominal > 300 eV analysis, it would require a threshold of 5.7 MeV, which would correspond to 4.2 MeV deposited into the thinner (0.38 mm) silicon of the array frame. This is consistent with the qualitative assessment that the SXS array was a factor of ~ 20 less sensitive to cosmic-ray impacts on the frame than XRS, for which the frame-event rate was comparable to the anti-co rate and the effective frame-event threshold was ~ 300 keV. The sensitivity is unlikely to be equal at all locations on the frame; the ground tests of putting alpha particles or heater pulses into a corner of the frame likely probed a less-sensitive location.

The heat sinking of SXS greatly suppressed the impact of frame events on the background compared with XRS, but the events well below trigger threshold still had an impact on the performance. Accumulating all of the calibration-pixel data into spectra sorted by COR, a small but significant correlation of resolution with cosmic-ray rate is seen (M. A. Leutenegger et al. in preparation), with the resolution ranging from 4.7 eV to 5.1 eV. Some of this

effect is due to the interaction of cosmic rays with the control thermometer, but the magnitude can be estimated from the housekeeping data and the measured dependence of resolution on temperature fluctuations. To gauge whether the rest of the dependence could be explained by untriggered frame events, we simulated 100000 X-ray events contaminated by frame events distributed in rate and amplitude according to the anti-co spectrum and count rate. For the pulse shape, we used the average of the smallest triggered frame events for which we had pulse records, and we scaled to energies in the anti-co spectrum assuming the reference pulse shape corresponded to 5.7 MeV. The resulting distortion of the simulated line shape was non-Gaussian, but if fitted with a Gaussian, resulted in a broadening term comparable to that observed in orbit after accounting for the effect of thermometer interference. The simulation was clearly oversimplified in its use of a single pulse shape, when in reality the pulse shape must depend on the location and energy of the input, but it suggests that frame events are likely the predominant cause of the dependence of resolution on COR.

The frame event pulses have thermal time constants of ~ 7 ms. The thermal conductance from the array to the detector board determined from static heating of test arrays ranged from $6\text{--}8 \times 10^{-7} \text{ WK}^{-1}$. Given the expected heat capacity of the added gold, the thermal time constant for the whole array die was expected to be ~ 1 ms, thus frame events would have been expected to have time constants similar to the pixel thermal time constant of ~ 4 ms. The discrepancy is not yet understood, but a detailed, three-dimensional, thermal model of the device has not been attempted.

3 Conclusion

We should not allow the preceding detail to obscure the fact that the SXS background was very low, enabling significant results to be obtained from very few photons in the SXS observations of N 132 D and IGR J16318–4848, which had been compromised by pointing problems (Hitomi Collaboration 2018a, 2018b). Even the most prominent line in the NXB, the Mn $K\alpha$, introduced only 92 photons in 366 ks. Only the Mn $K\alpha$ line was bright enough to serve as any sort of check on the energy scale, and only on the array in aggregate, not in individual pixels. The anti-coincidence detector performed as designed and removed signals from MIPs on individual pixels. The background was further reduced by characterizing pixel-to-pixel coincidences and using that information to refine the screening. These correlations appear to originate from various unrelated processes understood to greater and lesser extent. It is not necessary to understand them to screen them, but a more complete physical description of these events could assist in the design of future X-ray calorimeter instruments.

Acknowledgments

The authors gratefully acknowledge the many other scientists, engineers, technicians, and students whose hard work contributed

to the capabilities of the SXS. We acknowledge support from JSPS/MEXT KAKENHI grant numbers JP15H03642, JP16K05309, JP15K17657, JP15H05438, JP15H00785, and JP16H03954 and the Grant-in-Aid for Scientific Research on Innovative Areas: nuclear matter in neutron stars investigated by experiments and astronomical observations. U.S. authors gratefully acknowledge support through the NASA Science Mission Directorate.

References

- Boyce, K. R., et al. 1999, *Proc. SPIE*, 3675, 741
- Chiao, M. P., et al. 2016, *Proc. SPIE*, 9905, 99053M
- Eckart, M. E., et al. 2016, *Proc. SPIE*, 9905, 99053W
- Hitomi Collaboration 2018a, *PASJ*, 70, 16
- Hitomi Collaboration 2018b, *PASJ*, 70, 17
- Ishisaki, Y., et al. 2016, *Proc. SPIE*, 9905, 99053T
- Kelley, R. L., et al. 2007, *PASJ*, 59, S77
- Kelley, R. L., et al. 2016, *Proc. SPIE*, 9905, 99050V
- Kilbourne, C. A., Boyce, K. R., Brown, G. V., Cottam, J., Figueroa-Feliciano, E., & Fujimoto, R. 2006, *Nucl. Instrum. Methods Phys. Res., Sect. A*, 559, 620
- Kilbourne, C. A., et al. 2016, *Proc. SPIE*, 9905, 99053L
- Seta, H., et al. 2012, *IEEE Trans. Nuclear Sci.*, 59, 366
- Stahle, C. K., et al. 2004, *Nucl. Instrum. Methods Phys. Res., Sect. A*, 520, 472
- Takahashi, T., et al. 2016, *Proc. SPIE*, 9905, 99050U